Carbon 222 (2024) 118977

Contents lists available at ScienceDirect

Carbon

journal homepage: www.elsevier.com/locate/carbon

Directional charge transfer modulation in ultrathin polyporous carbon nitride nanotubes for enhanced peroxymonosulfate activation

Wenjin Cheng [a], Hao Liu [a], Guangfu Liao [b], Rongjie Wang [a,**], Xiaomei Zhao [c], Linxiang Zhou [a], Raul D. Rodriguez [a,d], Bin Yang [a,***], Xin Jia [a,*]

[a] School of Chemistry and Chemical Engineering/State Key Laboratory Incubation Base for Green Processing of Chemical Engineering, Shihezi University, Shihezi, Xinjiang, 832003, PR China
[b] College of Material Engineering, Fujian Agriculture and Forestry University, Fuzhou, 350002, PR China
[c] Key Laboratory of Theoretical Organic Chemistry and Functional Molecule, Ministry of Education, Hunan University of Science and Technology, Xiangtan, Hunan, 411201, PR China
[d] Tomsk Polytechnic University, 30 Lenin Avenue, 634050, Tomsk, Russia

ARTICLE INFO

Keywords:
Photocatalyst
Peroxymonosulfate
Carbon nitride
Interfacial built-in electric field
Imidacloprid
Degradation

ABSTRACT

Achieving enhanced degradation efficiency of the legacy pesticidal persistent organic pollutants in a photocatalysis coupling peroxymonosulfate activation (PC-PMS) system by boosting photogenerated carrier separation, remains considerable challenges. Herein, we delved into the directional charge transfer modulation of built-in electric field (BEF) within polyporous ultrathin carbon nitride nanotubes for strengthened PC-PMS mediated pesticide degradation. The ultrathin polyporous tubular nanostructure, are critical in shortening the diffusion pathways for the transport of photogenerated electron-hole pairs to the reaction interface, while simultaneously ensuring the abundant contact sites for the reaction medium. Additionally, the heptazine units containing amino groups served as oxidation centers under visible light, targeting the generation of reactive oxygen species of h^+, $O_2^{\bullet-}$, $^1O_2$. While the heptazine units containing cyano groups and boron dopants acted as reduction centers, activating PMS and O_2 to produce $SO_4^{\bullet-}$, •OH and $O_2^{\bullet-}$. The efficient generation of the radical species contributed to the ultrafast imidacloprid degradation in PC-PMS system. This study demonstrates that the combination of morphology and BEF engineering is a promising strategy for enhanced degradation efficiency of pesticide pollutants in the PC-PMS system.

1. Introduction

Imidacloprid (IMD) is one of the typical neonicotinoid pesticides widely employed in agriculture for pest and disease control. However, its high toxicity, long half-life, and propensity for bioaccumulation pose substantial threats to aquatic ecosystems and organisms. In this context, as an economical, eco-friendly, and efficient wastewater purification, the photocatalysis coupling peroxymonosulfate activation (PC-PMS) system is a promising approach to degrade and mineralize IMD pollutants by generating highly radical species [1–4]. Among the photocatalysts suitable for this application, metal-free graphitic carbon nitride ($g\text{-}C_3N_4$) nanotubes stands out due to its stable structure, scatter light effectively and distinctive nanoconfinement effect, making it an attractive choice for degrading refractory pollutants within the PC-PMS system [5,6]. However, pristine $g\text{-}C_3N_4$ nanotubes commonly were synthesized from cyanuric acid-melamine supramolecular assembly, feature thick tube walls, resulting in confined accessible surface area and sluggish charge dynamics, and thus, in relatively low catalytic activity [7]. Conversely, the ultrathin polyporous nature can provide a larger specific surface area, more exposed active sites, and shorter the perpendicular distance of photogenerated charges migrating towards the interface. Consequently, the conversion of the pristine $g\text{-}C_3N_4$ nanotubes to the ultrathin polyporous nanotubes should exhibit a significantly enhanced catalytic activity in PC-PMS system.

The high symmetry of heptazine structural units of $g\text{-}C_3N_4$ results in insufficient internal driving force, and slow separation and

* Corresponding author.
** Corresponding author.
*** Corresponding author.
E-mail addresses: wangrongjie@shzu.edu.cn (R. Wang), yangbin@shzu.edu.cn (B. Yang), jiaxin@shzu.edu.cn (X. Jia).

https://doi.org/10.1016/j.carbon.2024.118977
Received 30 November 2023; Received in revised form 30 January 2024; Accepted 26 February 2024
Available online 29 February 2024

transportation of photogenerated charge carriers, which is another important influence for hindering their catalytic activity. The built-in electric field (BEF) proved to be an effective strategy for driving the rapid separation of photogenerated charge carriers and directing their migration to independent active centers for enhanced redox efficiency [8–10]. Both constructing interface heterojunctions and breaking the symmetry of in-plane structural units are currently the most popular approaches to construct BEF for g-C_3N_4. Unfortunately, the former inevitably leads to recombination and energy loss of photogenerated charge carriers in the contact interface, while the latter leads to random or limited charge regions [11,12]. Recent researches have shown that grafting amino (-NH_2) groups within heptazine units can act as hole-stabilizers and thus prolong the lifetime of the excited states in g-C_3N_4 [13]. Furthermore, shen et al. revealed the synergy of cyano (-C ≡N) groups and boron (B) dopants in heptazine rings can achieve electrons enrichment [14]. Therefore, modifying –NH_2 groups on heptazine units as enrichment region of photogenerated holes, while introducing –C ≡N groups and B doping in another heptazine rings as enrichment region of photogenerated electrons, should be able to construct giant BEF.

Herein, we employed a stepwise thermal treatment to synthesize ultrathin polyporous g-C_3N_4 nanotubes (NBCN), which are composed of the heptazine units grafted with –NH_2 groups (N-heptazine) and the heptazine units co-modified with –C ≡N groups and B dopants (CB-heptazine). The ultrathin polyporous tubular nanostructure, which not only decreases the diffusion pathways for the transport of photogenerated electron-hole pairs to the reaction interface, but also ensures a high surface area with abundant contact sites for the reaction medium. Furthermore, the N-heptazine serves as the hole enrichment regions, and the CB-heptazine serves as the electron enrichment region, jointly constructing a giant BEF. The BEF leads to redistribution of electron density that restrains the recombination of photogenerated electron-hole pairs and increases the catalytic activity. Under visible-light irradiation, the component of N-heptazine served as oxidation centers, targeting the generation of radical species of h^+, $O_2^{\bullet-}$, $^1O_2$. While another component of CB-heptazine acted as reduction centers, activating PMS and O_2 to produce $SO_4^{\bullet-}$, •OH and $O_2^{\bullet-}$. Under constant attack from these radical species, the NBCN photocatalyst achieves 100% degradation of IMD within 20 min in PC-PMS system, which is 19 times than apparent degradation rate constant of the pristine g-C_3N_4. This work offers a new design idea for efficient g–C_3N_4–based photocatalysts for degradation of pesticidal pollutants.

2. Experimental

2.1. Synthesis of TCN

1 g of melamine was dissolved in 60 mL of aqueous solution at a dissolving temperature of 60 °C. Thereafter, the solution was transferred to a Teflon liner to react at 180 °C for 12 h. The obtained supramolecular precursor was filtered and washed several times and then dried at 50 °C. After that, 1 g of the supramolecular precursor was placed in a porcelain boat followed by pyrolysis at 550 °C for 4 h at a ramping rate of 5 °C min^{-1} under N_2 atmosphere in a tube furnace. The synthesized yellow product was g-C_3N_4 nanotubes, naming the TCN. The preparation of pristine g-C_3N_4 (PCN) is similar to TCN, melamine was pyrolyzed directly in a tube furnace under the same conditions.

2.2. Synthesis of BCN

0.4 g of TCN and 80 mg of $NaBH_4$ were mixed and grinded sufficiently. The mixture was placed in a porcelain boat with cover and calcined in tube furnace at 450 °C for 30 min at a ramp rate of 2.3 °C min^{-1} under N_2 atmosphere. The treated mixture was dispersed in 1 mol L^{-1} HCl solution and stirred vigorously for 5 min to fully remove the residual $NaBH_4$ and the lower HCl concentration and shorter treatment time are not sufficient to change the pore volume of the samples. The synthesized brown product was g-C_3N_4 nanotubes with –C ≡N groups and B dopants, nominating as BCN.

2.3. Synthesis of NBCN, NCN and BNCN

200 mg of BCN was placed in porcelain boat without cover and pyrolyzed in tube furnace at 495 °C for 1 h at a ramping rate of 5 °C min^{-1} under the NH_3 atmosphere. The synthesized dark brown product was thin-walled porous g-C_3N_4 nanotubes composed of N-heptazine and CB-heptazine, the samples were further pyrolyzed under NH_3 atmosphere based on BCN samples thus named NBCN. The preparation of g-C_3N_4 nanotubes with –NH_2 groups was obtained by the pyrolysis of TCN directly under ammonia atmosphere, named NCN. The synthesis of BNCN was similar to that of NBCN, except that the order of the two thermal treatments was reversed. 200 mg of NCN was mixed with 80 mg $NaBH_4$ followed by thermally reduced to obtain BNCN.

2.4. Sample characterizations

The scanning electron microscope (SEM) images and transmission electron microscope (TEM) images were recorded on FEI Quanta 250 FEG instrument (Veeco, USA). The high-resolution transmission electron microscopy (HRTEM) images were obtained on a JEM-2100 electron microscope (JEOL, Japan). The phase structure of the prepared samples was obtained by powder X-ray diffraction (XRD) measurements with monochromatic Cu Kα radiation (λ = 0.15418 nm) (Bruker D8 Advance). Fourier transform infrared (FTIR) spectra were recorded using a Bruker spectrometer (spectrum 2000) over the frequency range 2000–450 cm^{-1} at a resolution of 4 cm^{-1}. X-ray photoelectron spectroscopy (XPS) was recorded using a Thermo Scientific K-Alpha spectrometer with an Al Kα X-ray source and pass energy analyzer of 50 eV. The N_2 adsorption-desorption instrument (BET, Micromeritics APSP 2460) was used to analyze the specific surface area of the samples. Solid-state ^{13}C magic angle spinning (MAS) NMR measurements were obtained by a solid-state NMR spectrometer (Bruker 400W). The C and N element contents were determined on a Vario EL III elemental analyzer (EA). Ultraviolet–visible diffuse reflectance spectrum (UV–Vis DRS) was gained on a PerkinElmer Lambda 650S spectrometer. The photoluminescence (PL) spectra and time-resolved PL (TRPL) spectra were acquired by using an using an Edinburgh FLS980 spectrophotometer, whose excitation wavelength was set to 380 nm. AFM and KPFM are tested at Bruker Dimension ICON. Electron paramagnetic resonance (EPR) spectra were accepted on a Bruker EMXplus-6/1 spectrometer. The reflectance spectra of all samples over the 200–800 nm range were collected by a UV–visible spectrometer equipped with a Labsphere diffuse reflectance accessory (UV-2550, Shimadzu, Japan) and $BaSO_4$ is the reference standard. Elemental analysis (EA) was obtained by organic elemental analyzer (Elementar UNICUBE, Germany).

2.5. Photocatalytic degradation test

The performance of the prepared photocatalysts for activating PMS to degrade IMD was evaluated by using a 300 W xenon lamp (PLS-SME300E H1, Beijing Perfectlight) with 420 nm cut-off filter. As a procedure, 20 mg photocatalyst was dispersed in the reactor including 50 mL IMD aqueous solution (10 mg L^{-1}), which was kept at a constant temperature of 25 °C through a circulating cooling system. After adsorption for 30 min in a dark environment, 60 mg PMS was added into mixed solution and the light source was turned on. The distance between the light source and the liquid surface is set at 15 cm. At given time intervals, 1.5 mL aliquots were collected and then centrifuged and filtered by 0.22 μm polyethersulfone filter membrane. The residual concentration of IMD was analyzed via high performance liquid chromatograph (HPLC, Agilent 1260) with a UV detector at 270 nm and equipped with C18 column. The dispersed photocatalyst was collected

by suction filtration, washed four times with ethanol and water, and then tested for reusability. In addition, free radical capture experiments were conducted under the same conditions, during which TEMPO (5 mM), FFA (5 mM), TEOA (5 mM), MeOH (5 mM) and IPA (5 mM) were added to the solution to capture $\bullet O_2^-$, $^1O_2$, h^+, •OH and $\bullet SO_4^-$, •OH, respectively.

3. Results and discussion

3.1. Morphology and structure characterization

The stepwise thermal treatment involves the calcination of a mixture composed of g-C_3N_4 nanotubes and $NaBH_4$ in an inert atmosphere, followed by NH_3-mediated thermal exfoliation under an NH_3 atmosphere (Fig. 1a), Detailedly, the TCN and $NaBH_4$ were first subjected to thermal reduction at 450 °C for 30 min under the N_2 atmosphere to prepare BCN. In this process, the active hydrogen and boron atom released from $NaBH_4$ react with the N and C atoms in the g-C_3N_4 skeleton, where the –NH_3 groups decomposes and the C–N–C bond breaks to introduce –C ≡N groups [14]. Afterward, BCN was calcined at 495 °C for 60 min under the NH_3 atmosphere to generate the NBCN. On the one hand, the effect of NH_3 atmosphere makes the g-C_3N_4 nanotubes ultrathin and porous and the newly introduced pore structure gives more exposed edges, and on the other hand the intervention of NH_3 introduces more -NH_x at the edges of the g-C_3N_4 [15].

TEM (Fig. 1) and SEM (Fig. S1) images confirmed the successful preparation of the materials. TCN displayed a regular hexagonal tubular nanostructure with thick tube walls (Fig. 1b). The BCN exhibits a tubular morphology and wall thickness similar to TCN (Fig. 1c and Fig. S1d). After TCN is subjected to two steps of pyrolysis, the resultant NBCN was prepared, which maintains a hexagonal hollow tubular structure with a thin wall of about 41 nm (Fig. 1d and Fig. S1e). AFM similarly further confirms the transition of NBCN to an ultrathin nanotube structure (Fig. S2). A high-magnification TEM image clearly reveals the poly-porous structure of NBCN, which presents abundant in-plane holes with diameters ranging from tens to hundreds of nanometers (Fig. 1e).

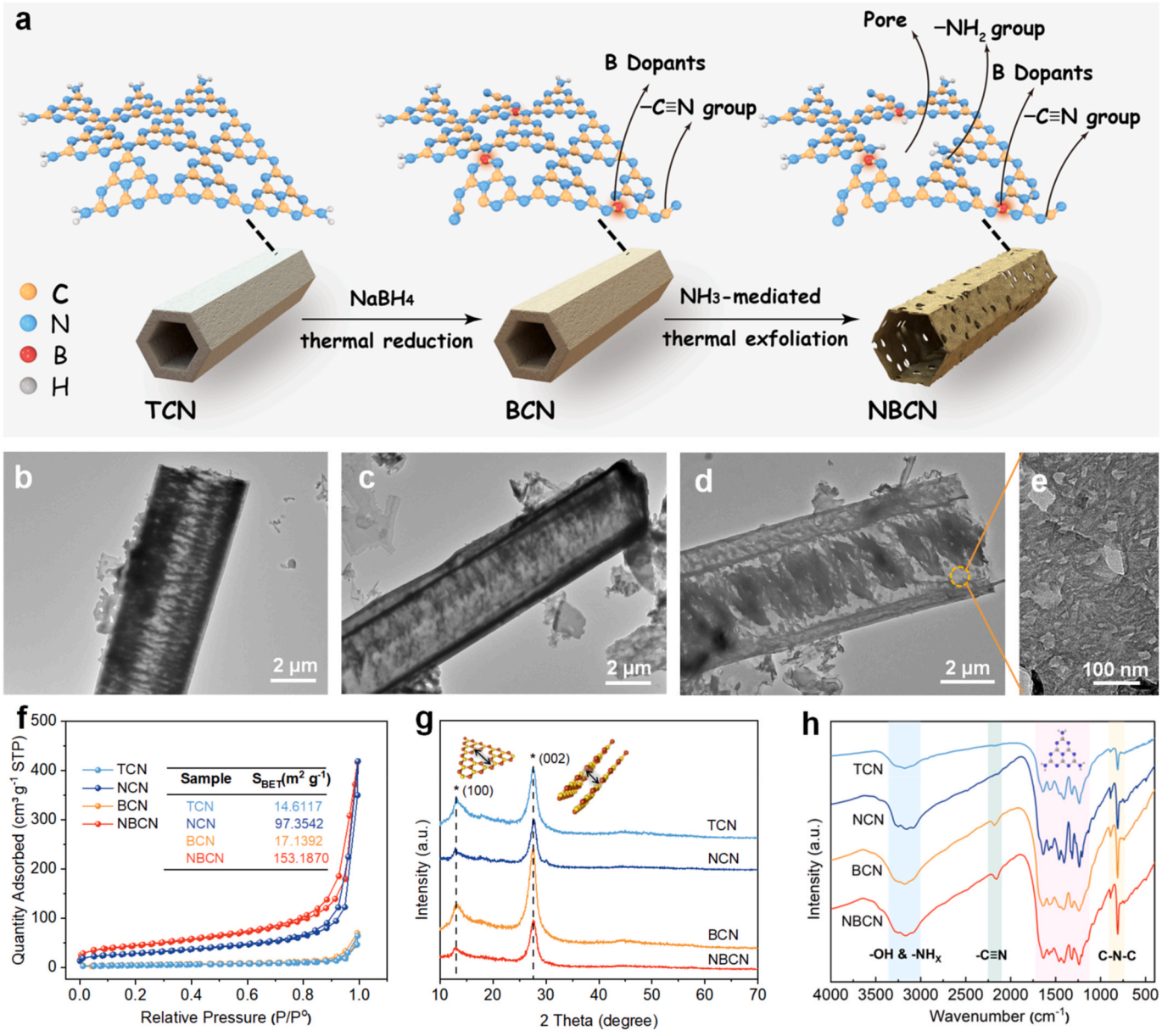

Fig. 1. (a) Schematic illustration of the synthesis process of NBCN; (b, c, d) TEM of TCN, BCN, and NBCN, respectively; (e) magnified TEM of NBCN, (f) N_2 adsorption-desorption isotherms curves, (g) XRD patterns, and (h) FTIR spectra of four samples. (A colour version of this figure can be viewed online.)

Energy-dispersive X-ray spectroscopy (EDS) mapping confirmed the uniform distribution of C, N, and B elements as well as the tubular nanostructure of NBCN (Fig. S3), confirming the successful B doping into heptazine rings.

The volume change sequence of the different samples with the same mass follows the order: TCN ≈ BCN < NCN < NBCN (Fig. S1l), which implies that the sample volumetric expansion is driven by NH_3-mediated thermal exfoliation rather than $NaBH_4$ thermal reduction. The BET was determined to be 153.19 $m^2\ g^{-1}$ for NBCN, which is over 10 times than that of TCN (14.61 $m^2\ g^{-1}$) (Fig. 1f). The pore size distribution analysis in Fig. S1l indicated the presence of micropores and mesopores in NBCN. These characterizations point to the unique ultrathin polyporous tubular morphology of NBCN [16–18].

The X-ray diffraction (XRD) patterns in Fig. 1g revealed that all samples exhibit characteristic (100) and (002) diffraction peaks at 13.1° and 27.5°, indicating the presence of heptazine units in the conjugated planes and a regular graphite-like interlayer stacking, respectively [19–21]. Compared with TCN and BCN, NCN and NBCN showed wider and weaker (100) and (002) peaks, suggesting their few-layer nature after undergoing NH_3-mediated thermal exfoliation [22].

The molecular structures of the four samples were revealed by FTIR (Fig. 1h). All g-C_3N_4 samples exhibited a sharp peak at 812 cm^{-1} that corresponds to the out-of-plane bending mode of heptazine rings, while the peaks in the 1100-1800 cm^{-1} region originate from the stretching modes of aromatic C–N bond within the heptazine rings. Additionally, many broad peaks around 3000-3500 cm^{-1} corresponding to the various -NH_x bond and –OH band stretching vibrations. BCN displayed an additional peak at 2170 cm^{-1} corresponding to the stretching vibration of the –C ≡N groups [23,24]. There is no sign of –C ≡N groups in NCN, which strongly supports our hypothesis that the –C ≡N groups do not originate from NH_3-mediated thermal exfoliation but $NaBH_4$ thermal reduction. In contrast, and what is critical to this work's objective, is the confirmation that NBCN retained these –C ≡N groups, proving that NH_3-mediated thermal exfoliation did not destroy CB-heptazine.

XPS provided insights into the surface chemistry of the photocatalysts. The C 1s high-resolution XPS spectra of TCN in Fig. 2a revealed the presence of sp^2 hybridized carbon (N–C═N), naked N ≡C/C–NH_x, and amorphous carbon (C–C/C═C), which were fitted into three peaks at 288.1 eV, 286.2 eV, and 284.6 eV, respectively [25–27]. The higher contribution of N ≡C/C–NH_x at 286.35 eV in NBCN (15.14%) with respect to TCN (4.47%), indicated the formation of abundant –NH_2 groups and –C ≡N groups due to the synergy effects of $NaBH_4$ thermal reduction and NH_3-mediated thermal exfoliation [28] (Fig. S5a). N 1s high-resolution XPS spectra of the TCN in Fig. 2d show the presence of C–N═C, N−$(C)_3$, and −NH_x peaks at 398.96 eV, 399.89 eV, and 401.59 eV, respectively. NCN showed a higher peak area ratio of C–N═C to N-$(C)_3$ than TCN (4.83 vs. 3.32) indicating the breaking of bridging N-$(C)_3$ and subsequent modification of –NH_2 groups [29] (Fig. S5b). BCN displayed a smaller C–N═C to N-$(C)_3$ ratio than TCN attributed to nitrogen defects introduced by the loss of nitrogen in the C–N═C and the formation of –C ≡N groups after TCN underwent $NaBH_4$ thermal reduction [5]. Meanwhile, NBCN showed a higher peak area ratio than BCN, proving that the NH_3-mediated thermal exfoliation did not destroy CB-heptazine, but can modify –NH_2 groups to form N-heptazine by breaking the bridging N-$(C)_3$. The B 1s high-resolution XPS spectra of all samples and solid-state ^{11}B CP-MAS-NMR spectrum of NBCN simultaneously demonstrate the successful doping of the B atom though replacing the apex carbon atom in the heptazine rings undergoing

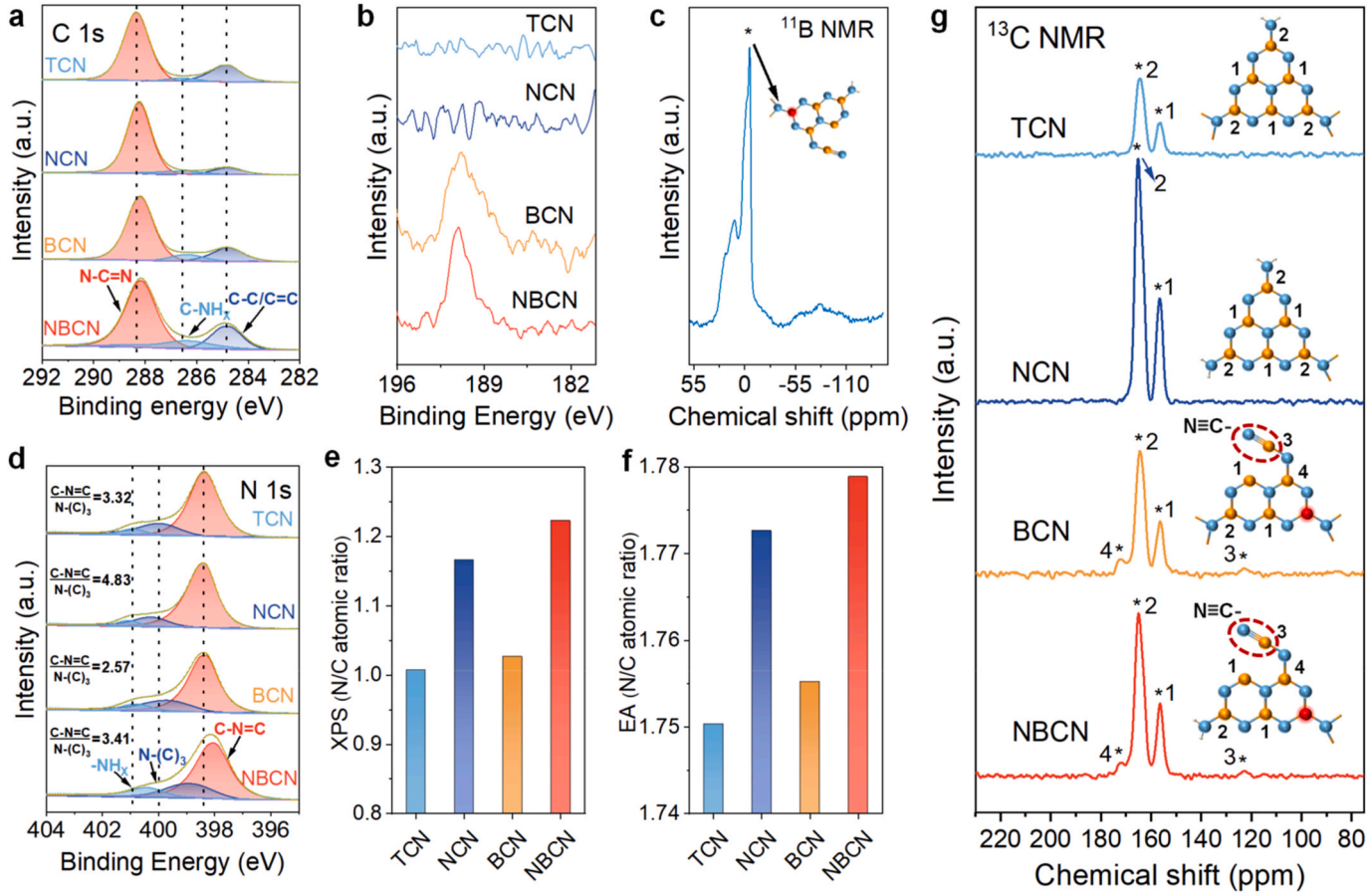

Fig. 2. (a, d) The C 1s and N 1s high-resolution XPS spectra of four samples; (b) The B 1s high-resolution XPS spectra of four samples and (c) solid-state ^{11}B CP-MAS-NMR spectra of NBCN; (e) N/C element content ratio of all samples obtained by XPS survey and (f) EA; (g) Solid-state ^{13}C NMR spectra of four samples. (A colour version of this figure can be viewed online.)

$NaBH_4$ thermal reduction [14,30] (Fig. 2b and c). In summary, our analysis indicates that $NaBH_4$ thermal reduction serves to construct CB-heptazine, while NH_3-mediated thermal exfoliation is responsible for the formation of N-heptazine.

EA is an intuitive quantitative method to characterize the element composition and content of the samples. Considering the trace doping of B, its effect on the C/N elemental ratio can be neglected. As shown in Fig. 2f, it is evident that the N/C element ratio is higher in NCN and NBCN compared to TCN and BCN, respectively. This result strongly indicates the successful modification of $–NH_2$ groups along the periphery of heptazine rings, which is consistent with the XPS surface analysis results (Fig. 2e and Fig. S4) [31–33].

Solid-state ^{13}C CP-MAS-NMR spectra confirmed the molecular structures of the samples. All samples present two peaks at 156.7 and 164.5 ppm corresponding to the characteristic C1 atoms in the $C–NH_x$ and C2 atoms in the N═C–N in the heptazine rings, respectively (Fig. 2g). The C2 to C1 peak intensity ratio showed significant changes. For TCN and BCN this ratio increased markedly, indicating the implantation of modified $–NH_2$ groups into the margins of heptazine rings [26,34]. In contrast, BCN showed a noticeable decrease in the C2 to C1 peak intensity ratio due to the introduction of –C ≡N groups and B dopants (Fig. S5d). Moreover, BCN displayed two new peaks at 171.6 and 122.8 ppm, corresponding to the neighboring less-intensity C4 peak and the nearly disappeared C3 peak of –C ≡N groups, which is attributed to B dopants at the C2 positions and the breaking of the N═C–N bonds at the C1 atoms (Fig. 2g) [14]. Remarkably, even after undergoing NH_3-mediated thermal exfoliation, the characteristic peaks of C3 and C4 are still present in NBCN. This provides strong evidence that NH_3-mediated thermal exfoliation does not damage the CB-heptazine.

UV-DRS results in Fig. 3a evidence the optical absorption properties of our four samples [25,35,36]. Notably, the brown BCN shows a significant red shift in its light absorption edge compared to the yellow TCN. In contrast, the light absorption edge of beige NCN is blue-shifted relative to that of TCN, which we attribute to quantum confinement effect by the polyporous and ultrathin tubular architecture. Moreover, the dark brown NBCN has a broader and stronger light absorption edge compared to other samples. This enhanced absorption can be attributed to the synergistic effects between the quantum confinement effects caused by the porous and ultrathin tubular nanoarchitecture, and the construction of BEF [37]. These findings confirm that NBCN efficiently harvests visible light, making it well-suited for subsequent catalytic reactions. The band structures of the four samples were obtained based on Tauc curves and valence band XPS spectra, see details in Fig. S6. Obviously, the synergistic effect of B dopants/–C ≡N groups and ultrathin tubular structure effectively optimizes the electronic band structure and promotes the effective absorption of visible light, which is beneficial to improve photocatalytic efficiency [30,38].

We conducted photoelectrochemical experiments to investigate the separation and migration behavior of photogenerated electron-hole pairs [39,40]. In multiple cycles under switching visible-light illumination, NBCN exhibits the highest photocurrent signal intensity, indicating the most efficient separation of photogenerated electron-hole pairs (Fig. 3b) [41–44]. Considering the excellent visible-light absorption of NBCN, we conducted photocurrent tests at different wavelengths. The results shown in Fig. S7, reveal that NBCN exhibits a photocurrent response even under a wide spectral range of visible light. Furthermore, we observed that the photocurrent intensity of NBCN decreased sharply with the addition of PMS under visible light (Fig. S8). This decrease indicates the inhibition of photogenerated electrons and holes recombination in the presence of PMS. This is due to PMS acting as an electron acceptor that rapidly traps photogenerated electrons, contributing to the enhanced photocatalytic activity [45]. NBCN exhibits the smallest arc radius of all samples as deduced from electrochemical impedance spectra (EIS) in Fig. 3c. This observation suggests enhanced conductivity and photocarrier mobility in NBCN, further supporting its superior photocatalytic performance [46,47]. The electrochemically active surface area (ECSA) based on the results of double layer capacitance (C_{dl}) tested by cyclic voltammetry (CV) (Fig. S9). Compared to TCN, NBCN have a larger slope of fitting potential versus current density curves at different scan rates, suggesting that NBCN with a bigger ECSA can

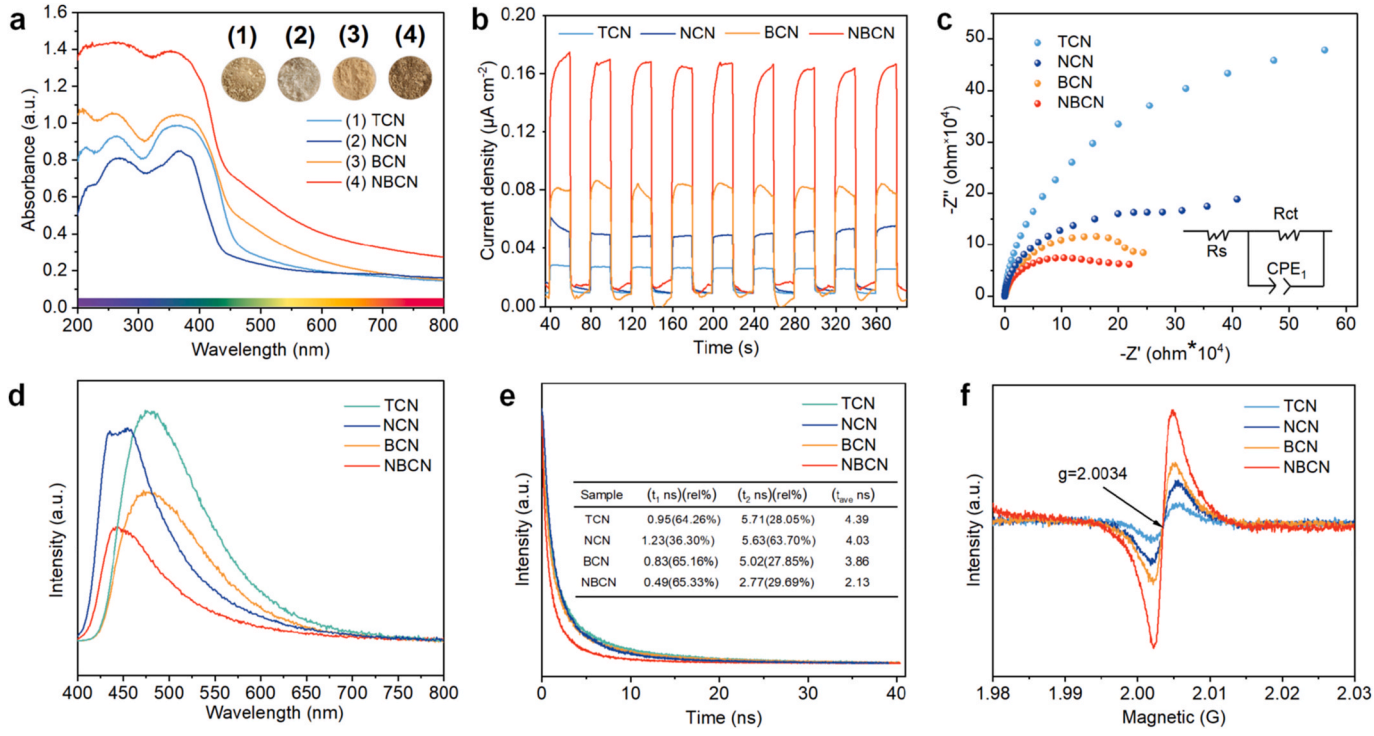

Fig. 3. (a) UV-DRS and (b) switching photocurrent responses of samples under λ ≥ 420 nm visible light; (c) Nyquist plot of EIS; (d) The steady-state PL emission spectra, and (e) time-resolved PL decay spectra of different samples (excitation wavelength 380 nm); (f) EPR spectra. (A colour version of this figure can be viewed online.)

provide more active sites for photocatalytic reaction [48,49].

We further investigated the separation and migration properties of photogenerated electron-hole pairs by steady-state PL emission spectra [50,51], as shown in Fig. 3d. Compared to TCN, NCN and BCN, NBCN exhibits a weak PL emission peak indicating excellent separation and migration of photogenerated electron-hole pairs. This is attributed to the synergistic effect of the polyporous and ultrathin tubular architecture as well as giant BEF [5,52]. Meanwhile, the PL emission peak of NBCN and NCN all showed a significant blue shift relative to TCN and BCN. This shift is attributed to the reduced conjugation length and strong quantum confinement effect caused by the polyporous and ultrathin properties after NH_3-mediated thermal exfoliation. The TRPL spectra show that the emission lifetime of NBCN is much shorter than TCN, NCN and BCN (Fig. 3e). This shortened average lifetime of photogenerated electron-hole pairs is attributed to the promotion of exciton dissociation caused by the giant BEF [20,53].

EPR spectra shown in Fig. 3f indicated that all four samples present a single Lorentzian line located at a g value of around 2.003. The EPR signal was much higher for BCN and NCN compared to TCN and was highest for NBCN. This increased EPR intensity in NBCN implies an increase of unsaturated sites. Thus, it is favorable for the generation of photo-induced carriers, which would directly participate in the

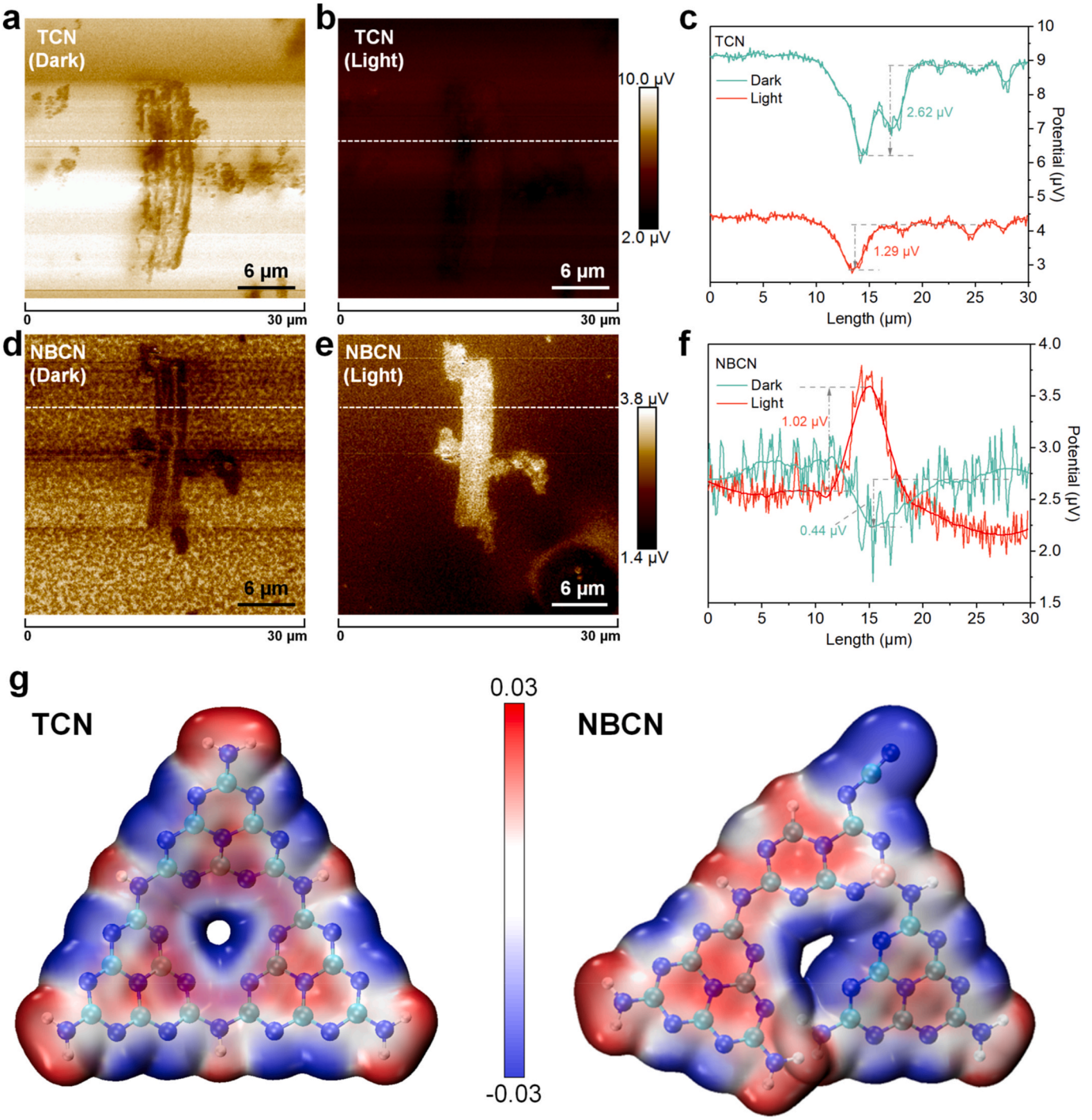

Fig. 4. KPFM potential data of TCN, NBCN in the (a, d) dark, and (b, e) illumination, and (c, f) the corresponding surface potential curves; (g) The surface electrostatic potentials of TCN and NBCN. (A colour version of this figure can be viewed online.)

generation of reactive oxygen species to degrade pollutants in the PC-PMS system (Fig. 3f) [14,54–56].

The surface potential of the synthesized catalysts was measured by in situ irradiated kelvin probe force microscopy (KPFM) to elucidate the formation of the BEF. The surface potentials distribution was tested under dark and light conditions, respectively. As shown in Fig. 4c, the TCN potential difference decreased from 2.62 μV to 1.29 μV, which indicates that the charge response of the TCN weakened under illuminated conditions [57]. Meanwhile, the surface potential of the NBCN is lower than that of the substrate under dark conditions, with a difference of 0.44 μV. But under light conditions, the surface potential of NBCN was obviously increased with a potential difference of 1.02 μV, suggesting that a strong built-in electric field exists between the molecular units of NBCN (Fig. 4f).

In order to further reflect the presence of giant BEF, the surface electrostatic potential of materials was analyzed by theoretical calculations. The electrostatic potential distribution of NBCN changes considerably, which becomes extremely asymmetric compared to TCN (Fig. 4g). Considering the strong electron-withdrawing property of both –C ≡N groups and the regulation of localized charge distribution by B dopants, the negative electrostatic potential is mainly distributed on the CB-heptazine, while the positive electrostatic potential is mostly concentrated at the N-heptazine because of the ability of $–NH_2$ groups to enrich photogenerated holes. The result forcefully demonstrates the formation of a giant BEF between the adjacent heptazine rings in the NBCN, which can significantly promote photoinduced exciton formation and spatial separation of charges [58,59].

3.2. Degradation properties for IMD

To evaluate the catalytic properties of the different samples, we conducted photocatalytic degradation experiments of IMD using different samples under visible light. As shown in Fig. S22, only 0.4% of IMD was adsorbed by NBCN under 3 h of dark conditions, and the effect of adsorption of IMD was not significant compared to other samples, suggesting that the decrease in IMD concentration is not caused by adsorption, but by photocatalysis. Fig. 5a shows almost no photodegradation in the absence of sample. Notably, NBCN exhibited the highest photocatalytic degradation activity among all samples (Fig. 5a). The degradation rate constant (K) for NBCN was measured at 0.026 min^{-1}, which is 10.4, 3.5, 2.2, and 2.0 times higher than that of pristine g-C_3N_4 (PCN), TCN, NCN, and BCN, respectively (Fig. 5b). When compared to reported photocatalysts, NBCN still demonstrated better photocatalytic performance for IMD degradation (see Table S3). However, it is worth noting that the photocatalytic degradation efficiency of IMD using NBCN, while impressive, is still relatively low, requiring up to 90 min to achieve 91% degradation of IMD, which may not be ideal for practical applications.

To further improve the removal efficiency of IMD, we performed degradation experiments using different samples in a PC-PMS system under illumination. As shown in Fig. S23a, when NBCN and PMS coexisted without illumination, only 16% of IMD was removed within 20 min. In contrast, PMS alone achieved only 18% IMD removal within the same time under visible light, indicating the poor reactivity of PMS activation by either visible light or NBCN alone. When both visible light and PMS were present, the NBCN in the PC-PMS system can achieve 100% IMD removal in 20 min with a K value of 0.21 min^{-1}. This rate constant is significantly higher among all other samples, being as much as 19.1, 7.0, 4.2, and 3.0 times that of PCN, TCN, NCN, and BCN, respectively (Fig. 5c and d). The PC-PMS system has a K value for IMD degradation that is 7.78 times higher than the photocatalytic system alone. These results demonstrate that there is a strong the synergistic effect between NBCN and PMS under irradiation, greatly enhancing the efficiency of IMD degradation. Moreover, NBCN exhibited a higher removal ability of IMD than BNCN prepared by NH_3-mediated thermal exfoliation and subsequent $NaBH_4$ thermal reduction. It may be

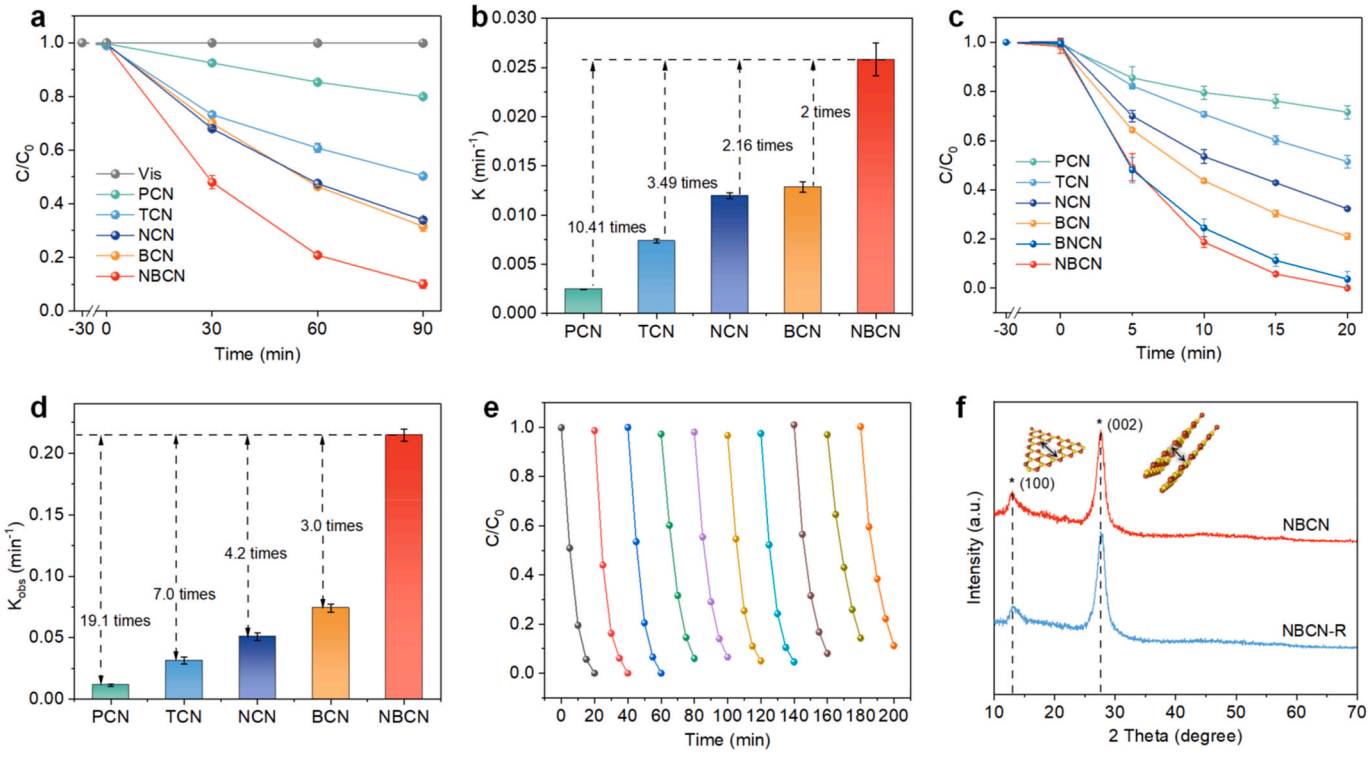

Fig. 5. Photocatalytic degradation curves (a) and corresponding K values (b) based on the photocatalytic degradation of IMD over different samples without PMS under visible light irradiation; Degradation curves (c) and corresponding K values (d) of IMD in PC-PMS system under illumination; (e) Cycling stability of the NBCN under λ ≥ 420 nm visible light, and (f) XRD of NBCN before and after ten cycles (The sample after ten cycles is marked as NBCN-R). (A colour version of this figure can be viewed online.)

attributed to the post-processing sequence influences the specific surface area of materials The decrease in specific surface area may be attributed to the secondary polymerization of amino-rich NCN during the subsequent pyrolysis with $NaBH_4$ (Fig. S12). This finding indicates that the highest activity of g-C_3N_4 nanotubes can only be achieved by first performing $NaBH_4$ thermal reduction followed by NH_3-mediated thermal exfoliation. When compared to reported photocatalysts, NBCN still demonstrates superior IMD degradation activity in the PC-PMS system under illumination (see Table S4).

To demonstrate the potential of NBCN in utilizing wide-range visible light, we performed IMD degradation experiments in a wide-spectrum-driven PC-PMS system. As shown in Figs. S13–17, NBCN was capable of completely removing IMD within only 5 min in the PC-PMS system under illumination ranging from 780 nm down to 380 nm. Its degradation rate constant K was 7 times higher than that of TCN. Even when the system was exposed to $\lambda \geq 510$ nm visible light, IMD removal still reached 29% within 60 min, which is much higher than TCN.

The stability and reusability of catalysts are crucial factors in their evaluation. Therefore, we tested the recyclability of NBCN over 10 consecutive cycles. As presented in Fig. 5e, even after 10 cycles the IMD degradation rate remains at 89%. This result indicates that NBCN has good stability and reusability as a catalyst [60]. In addition, the XRD, FTIR and XPS characteristic peak positions of the used NBCN are similar to those of the fresh sample, and TEM and SEM images of the used NBCN show that the sample still preserves its original polyporous and ultrathin tubular architecture. These findings provide further evidence of the excellent recyclability of NBCN in the PC-PMS system (Fig. 5f and Fig. S18).

To further demonstrate the practical application potential of NBCN in the PC-PMS system, we conducted large-scale experiments under actual outdoor sunlight using 5 L of tap water containing 10 mg L^{-1} IMD, 0.04 g/L NBCN, and 0.24 g/L PMS. Remarkably, we achieved a 91% degradation of IMD in just 180 min of sunlight exposure. (Figs. S20 and 21). This highlights the potential practical applications of NBCN in real-world scenarios. Fig. S25 reflects the evolution of IMD and intermediates by comparing the chromatograms of different degradation times in PC-PMS system. The chromatogram for TCN at 0 min shows the only high intensity peak corresponding to the characteristic peak of IMD. There were obvious characteristic peaks of other intermediates at 30 min, and with the extension of time, the area of the characteristic peak of IMD decreased. However, the characteristic peaks of the other intermediates were still present and did not have a significant decreasing trend (Fig. S25a). The characteristic peaks of IMD for NBCN completely disappeared at 30 min, and the characteristic peak areas of the intermediates showed a trend of increasing and then decreasing with the degradation time. The characteristic peaks of all intermediates almost completely disappeared at 120 min, which indicated that the PC-PMS system using NBCN achieved complete mineralization of IMD at 120 min (Fig. S25b). Considering the significant impact of reaction conditions on the IMD degradation process, we conducted a thorough investigation of the effect of different reaction conditions. These included the dose of catalyst and PMS, IMD concentration, initial pH value, temperature, inorganic anions, organic substances, and different actual water samples. Detailed data analysis and discussion based on these multiparametric experiments are presented in the Supporting Information on pages 30–33.

3.3. Study on the catalytic mechanism

In order to identify the main radical species responsible for IMD degradation in the PC-PMS system under visible light using NBCN as the photocatalyst, the impact of different trapping agents on the degradation process (Fig. 6a). The results showed that TEMPO, FFA, and TEOA significantly inhibited the degradation of IMD, with inhibition rates of 98.5%, 97.9%, and 82.6%, respectively. This suggests that $\bullet O_2^-$, $^1O_2$, and h^+ play a major role in the degradation process. On the other hand, MeOH and IPA showed lower inhibition rates of 61.6% and 32.7%, respectively, indicating that •OH, and $\bullet SO_4^-$ played a secondary role in the degradation of IMD (Fig. 6b). To further understand the mechanization of PMS activation, the dissolved O_2 in the PC-PMS system was

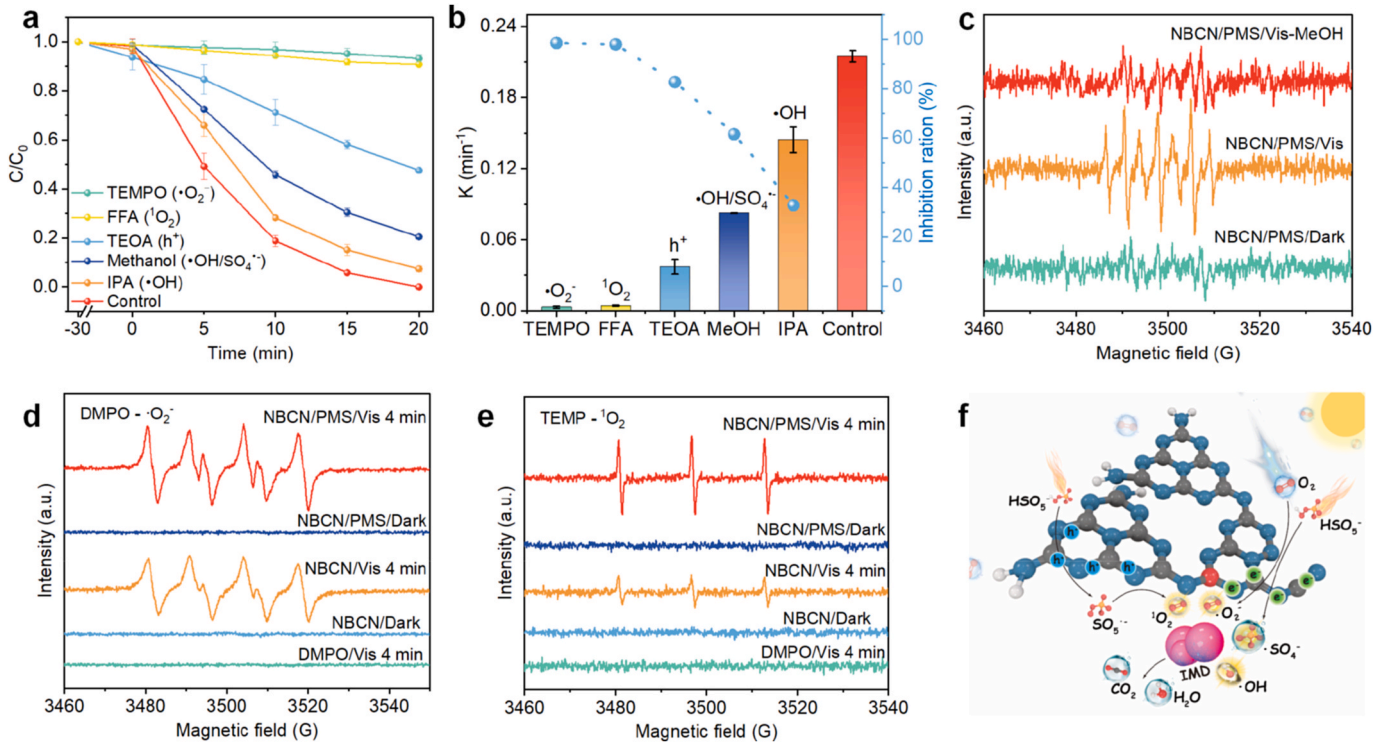

Fig. 6. (a, b) Effect of scavengers on IMD degradation, and (c–e) spin-trapping EPR spectra; (f) The possible photocatalytic mechanisms in the PC-PMS system. (A colour version of this figure can be viewed online.)

eliminated by introducing an argon gas [1,61]. The results shown in Fig. S26 indicated that the removal of IMD is only slightly inhibited after the introduction of argon gas into the PC-PMS system. However, the removal of IMD was dramatically inhibited after the introduction of argon into the photocatalysis system. This result indicates that $\bullet O_2^-$ and $^1O_2$ mainly originate from the activation and transformation of PMS rather than dissolved O_2, and the slight inhibition of IMD removal in the PC-PMS system can be attributed to photocatalysis.

The EPR spectra were used to further confirm the types of radical species in the PC-PMS system. The EPR spectra in Fig. 6c were obtained from a deionized water system with DMPO as a spin trapping agent. Under dark conditions, characteristic peaks of 5,5-dimetphylpyrroline-(2)-oxyl-(1) (DMPOX) with an intensity ratio of 1:2:1:2:1:2:1 are observed, which can be attributed to the direct oxidation of DMPO by $\bullet OH$ and $\bullet SO_4^-$ [62–64]. Importantly, under illumination, the peak intensity of DMPOX is significantly enhanced because more $\bullet OH$ and $\bullet SO_4^-$ are produced by the activation of PMS. However, the intensity of the characteristic peak of DMPOX in the MeOH system is weakened, likely due to the quenching effect of MeOH on the two free radicals, which also confirms the appearance of $\bullet OH$ and $\bullet SO_4^-$. As shown in Fig. 6d, the characteristic signal of DMPO-$\bullet O_2^-$ does not appear in the dark, NBCN/dark, and NBCN/PMS/dark conditions. In contrast, a distinct characteristic signal of DMPO-$\bullet O_2^-$ appears under the NBCN/light condition, and this signal peak is stronger under the NBCN/PMS/light condition. This observation is attributed to the high concentration of $\bullet O_2^-$ generated by the synergistic effect of photocatalysis and PMS activation (Fig. 6d) [52,65–67]. Fig. 6e presents a triplet signal characteristic of TEMP-$^1O_2$ with approximately equal intensity, indicating the formation of $^1O_2$ in the NBCN/light condition. Moreover, the strongest signal peaks of TEMP-$^1O_2$ emerge in the NBCN/PMS/light condition, indicating a higher concentration of $^1O_2$ generated by PMS activation. In summary, these findings show that the coupling of photocatalysis and PMS activation is the key approach to effectively generate radical species, which play essential roles in the degradation of IMD.

The proposed catalytic mechanism based on the experimental results can be summarized as follows. In the PC-PMS system, both photocatalysis and PMS activation are the main reactions. NBCN is excited under illumination, producing photogenerated electrons (e^-) and holes (h^+) pairs travel to N-heptazine and CB-heptazine to separate and enrich, respectively. The e^- and h^+ mainly participates in follow reactions. First, the e^- reacts with dissolved O_2 to generate $\bullet O_2^-$ (Eq. (1)), as the reduction potential of $O_2/\bullet O_2^-$ is lower than the CB potential of NBCN. Second, PMS (HSO_5^-) receives e^- and is activated to generate $\bullet SO_4^-$ and $\bullet OH$, as described by Eq. (2) and Eq. (3), respectively [3]. Additionally, the h^+ reacts with PMS (HSO_5^-) to produce $SO_5^{\bullet-}$ (Eq. (4)) or directly degrade pollutants. Thereafter, $SO_5^{\bullet-}$ subsequently undergoes self-decay to produce $^1O_2$, or reacts with H^+ to produce the intermediate HO_2^-, which further decomposes to produce $\bullet O_2^-$ (Eqs. (5)–(7)) [63,68]. Additionally, the $\bullet O_2^-$ can also be directly oxidized by holes to $^1O_2$ (Eq. (8)) [3]. This proposed mechanism explains how both photocatalysts and PMS activation generate various radical species (Fig. 6f).

$$O_2 + e^- \rightarrow \bullet O_2^- \quad (1)$$

$$HSO_5^- + e^- \rightarrow \bullet OH + SO_4^{2-} \quad (2)$$

$$HSO_5^- + e^- \rightarrow OH^- + \bullet SO_4^- \quad (3)$$

$$HSO_5^- + h^+ \rightarrow SO_5^{\bullet-} + H^+ \quad (4)$$

$$2SO_5^{\bullet-} \rightarrow 2SO_4^- + {}^1O_2 \quad (5)$$

$$SO_5^{\bullet-} + H^+ \rightarrow SO_3 + \bullet HO_2^- \quad (6)$$

$$\bullet HO_2^- \rightarrow H^+ + \bullet O_2^- \quad (7)$$

$$\bullet O_2^- + h^+ \rightarrow {}^1O_2 \quad (8)$$

DFT calculations were used to analyze the regioselectivity of free radical attacks on IMD, which can provide valuable theoretical insights into predicting the degradation pathway of IMD. In this work, the Fukui index (f^0) was calculated based on natural population analysis (NPA) charge, where higher f^0 values indicate susceptibility to free radical attacks [69,70]. Generally, the HOMO orbitals represent electrons that are more readily available for escape and are vulnerable to free radical attack, and the HOMO orbit of IMD is concentrated near the imidazole ring (Figs. S28a and b) [71–73]. Corresponding to the condensed Fukui function and atomic coloring diagram of different values of f^0, the strong f^0 values of the 15 N, and 8 N atoms on the imidazole ring implicate that they are the most likely for radical species attack (Figs. S28d–f).

To elucidate the degradation pathways of IMD, intermediates were identified using liquid chromatography-mass spectrometry. The mass spectrometry information for the degradation intermediates is provided in Table S5 and Fig. S29. As shown in Scheme 1, the degradation process is divided into three main pathways (D1, D2, and D3). In the D1 pathway, the parent compound IMD (P1) undergoes dehydrogenation and hydroxylation to form P2, which is then further hydroxylated to produce P4 [74]. Afterward, P4 is oxidized to P5, and another pathway converts P4 into P6 by removing -N-NO_2 [75]. In this process, P5 and P6 undergo N-dealkylation of the amine under the attack of radicals, leading to the formation of P7, P8, P9, and P10. This result is consistent with the fact that the 8 N atom on the imidazole ring with a high Fukui functional index (0.068) is susceptible to attack by free radicals [3]. In the D2 pathway, IMD is subjected to hydroxylation and oxidation to form P3, which is further decomposed into smaller molecular products, eventually converting to CO_2 and H_2O. In the D3 pathway, IMD is converted directly into P7, P8, P9, and P10 under the attack of radical species. The high f^0 of 19 O, 20 O, and 8 N in the -N-NO_2 group corresponds to their high susceptibility to attack by radical species, supporting the possibility of the D3 pathway.

The ECOSAR program was used to evaluate the acute and chronic toxicity of IMD and its by-products to fish and plankton (daphnia). The concentrations of acute and chronic toxicity are classified as extremely toxic, toxic, harmful, and harmless (Scheme 1; Tables S6 and 7) [76,77]. In the PC-PMS system, IMD, P2, and P3 show relatively high acute and chronic toxicity. However, as the degree of oxidation and cleavage of the by-products continue to increase, the acute and chronic toxicity of other by-products noticeably decreases. In summary, the final by-products of IMD degradation are eco-friendly and cause much less harm to the ecosystem than the parent compound.

4. Conclusion

This study successfully synthesized a polyporous ultrathin g-C_3N_4 nanotubes composed of N-heptazine and CB-heptazine through a facile stepwise thermal treatment process. This new photocatalyst exhibits 100% degradation of IMD within 20 min in PC-PMS system, along with excellent stability and reusability, which is superior to most reported catalysts. The improved catalytic activity of NBCN can be attributed to the ultrathin polyporous tubular nanostructure, which not only inhibits the interior recombination of photogenerated electron-hole pairs, but also ensures the abundant contact sites for the reaction medium. Additionally, the formation of BEF between N-heptazine and CB-heptazine restrains the recombination of photogenerated charge carriers, and enhanced spatial isolation of oxidation and reduction dual centers to produce the radical species, which further contributed to its boosted photocatalytic activity. This work demonstrates a promising strategy for the rational morphological engineering and BEF design of g-C_3N_4 photocatalysts, leading to the highly efficient degradation of refractory contaminants in a PC-PMS system.

CRediT authorship contribution statement

Wenjin Cheng: Conceptualization, Data curation, Formal analysis,

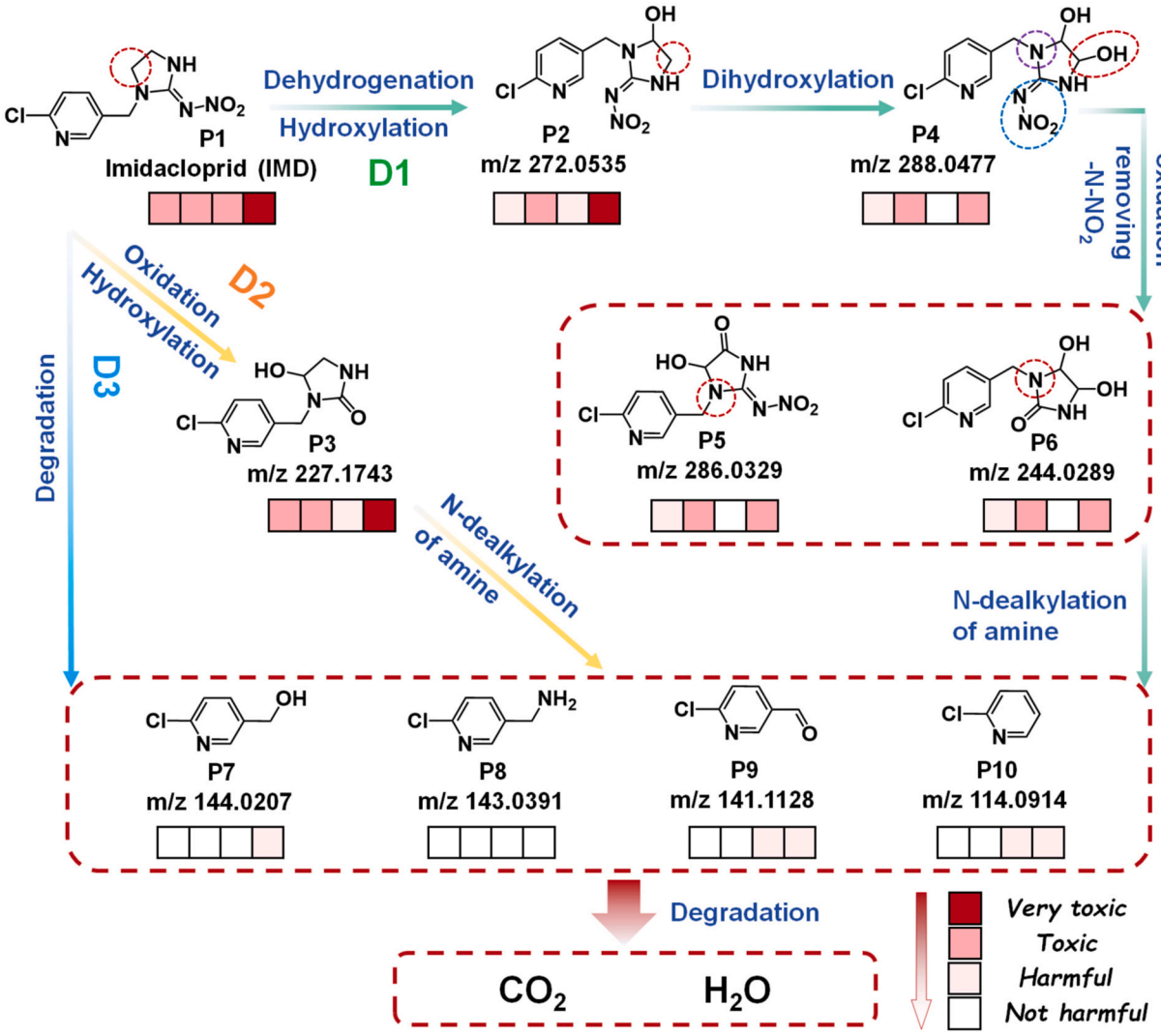

Scheme 1. Degradation pathway analysis of IMD in the PC-PMS system, and toxic evolution of intermediates in the three degradation pathways evaluated by ECOSAR. The four different shades of red below each intermediate represent their acute and chronic toxicity to fish and daphnia, from left to right.

Investigation, Methodology, Project administration, Resources, Software, Supervision, Validation, Visualization, Writing – original draft, Writing – review & editing. **Hao Liu:** Conceptualization, Formal analysis. **Guangfu Liao:** Investigation, Writing – review & editing. **Rongjie Wang:** Supervision. **Xiaomei Zhao:** Software, Visualization. **Linxiang Zhou:** Software, Visualization. **Raul D. Rodriguez:** Supervision, Writing – review & editing. **Bin Yang:** Conceptualization, Formal analysis, Funding acquisition, Investigation, Methodology, Project administration, Resources, Software, Supervision, Validation, Visualization, Writing – review & editing. **Xin Jia:** Formal analysis, Funding acquisition, Investigation, Methodology, Project administration, Resources, Software, Supervision, Validation, Visualization, Writing – review & editing.

Declaration of competing interest

The authors declare that they have no known competing financial interests or personal relationships that could have appeared to influence the work reported in this paper.

Acknowledgements

This study was supported by the National Natural Science Foundation of China (22308223, U1703351, 52073179), the High-level Talents launching Project (RCZK202328), Tianshan Talent Support Program for Xin Jia, and the Program of Introducing Talents of Discipline to Universities (D20018). We would like to thank the Analysis and Testing Center of Shihezi University, ceshigo (www.ceshigo.com) and Shiyanjia lab (www.shiyanjia.com) for providing assistance in characterizations. RDR also thanks the RFBR and DFG, project number 21-53-12045.

Appendix A. Supplementary data

Supplementary data to this article can be found online at https://doi.org/10.1016/j.carbon.2024.118977.

References

[1] H. Ming, P. Zhang, Y. Yang, Y. Zou, C. Yang, Y. Hou, K. Ding, J. Zhang, X. Wang, Tailored poly-heptazine units in carbon nitride for activating peroxymonosulfate to degrade organic contaminants with visible light, Appl. Catal. B Environ. 311 (2022) 121341.

[2] F. Chen, L.-L. Liu, J.-H. Wu, X.-H. Rui, J.-J. Chen, Y. Yu, Single-atom iron anchored tubular g-C_3N_4 catalysts for ultrafast fenton-like reaction: roles of high-valency iron-oxo species and organic radicals, Adv. Mater. 34 (2022) 2202891.

[3] J. Tan, Z. Li, J. Li, Y. Meng, X. Yao, Y. Wang, Y. Lu, T. Zhang, Visible-light-assisted peroxymonosulfate activation by metal-free bifunctional oxygen-doped graphitic carbon nitride for enhanced degradation of imidacloprid: role of non-

photochemical and photocatalytic activation pathway, J. Hazard Mater. 423 (2022) 127048.
[4] J. Matos, S. Miralles-Cuevas, A. Ruíz-Delgado, I. Oller, S. Malato, Development of TiO_2-C photocatalysts for solar treatment of polluted water, Carbon 122 (2017) 361–373.
[5] Y. Xiao, G. Tian, W. Li, Y. Xie, B. Jiang, C. Tian, D. Zhao, H. Fu, Molecule self-assembly synthesis of porous few-layer carbon nitride for highly efficient photoredox catalysis, J. Am. Chem. Soc. 141 (2019) 2508–2515.
[6] W. Tao, Q. Tang, J. Hu, Z. Wang, B. Jiang, Y. Xiao, R. Song, S. Guo, Construction of a hierarchical BiOBr/C_3N_4 S-scheme heterojunction for selective photocatalytic CO_2 reduction towards CO, J. Mater. Chem. A 11 (2023) 24999–25007.
[7] S. Guo, Z. Deng, M. Li, B. Jiang, C. Tian, Q. Pan, H. Fu, Phosphorus-Doped carbon nitride tubes with a layered micro-nanostructure for enhanced visible-light photocatalytic hydrogen evolution, Angew. Chem. Int. Ed. 55 (5) (2016) 1830–1834.
[8] J. Low, J. Yu, M. Jaroniec, S. Wageh, A.A. Al-Ghamdi, Heterojunction photocatalysts, Adv. Mater. 29 (20) (2017) 1601694.
[9] Y. Zhu, J. Ren, G. Huang, C.-L. Dong, Y.-C. Huang, P. Lu, H. Tang, Y. Liu, S. Shen, D. Yang, Red phosphorus grafted high-index (116) faceted anatase TiO_2 for Z-scheme photocatalytic pure water splitting, Adv. Funct. Mater. 2311623.
[10] G. Liao, G. Ding, B. Yang, C. Li, Challenges in Photocatalytic Carbon Dioxide Reduction, Precision Chemistry, 2024.
[11] B. Yan, C. Du, G. Yang, Constructing built-in electric field in ultrathin graphitic carbon nitride nanosheets by N and O codoping for enhanced photocatalytic hydrogen evolution activity, Small 16 (4) (2020) 1905700.
[12] A. Deng, Y. Sun, Z. Gao, S. Yang, Y. Liu, H. He, J. Zhang, S. Liu, H. Sun, S. Wang, Internal electric field in carbon nitride-based heterojunctions for photocatalysis, Nano Energy 108 (2023) 108228.
[13] N. Meng, J. Ren, Y. Liu, Y. Huang, T. Petit, B. Zhang, Engineering oxygen-containing and amino groups into two-dimensional atomically-thin porous polymeric carbon nitrogen for enhanced photocatalytic hydrogen production, Energy Environ. Sci. 11 (3) (2018) 566–571.
[14] D. Zhao, C.-L. Dong, W. Bin, C. Chen, Y.-C. Huang, Z. Diao, S. Li, L. Guo, S. Shen, Synergy of dopants and defects in graphitic carbon nitride with exceptionally modulated band structures for efficient photocatalytic oxygen evolution, Adv. Mater. 31 (2019) 1903545.
[15] N. Meng, J. Ren, Y. Liu, Y. Huang, T. Petit, B. Zhang, Engineering oxygen-containing and amino groups into two-dimensional atomically-thin porous polymeric carbon nitrogen for enhanced photocatalytic hydrogen production, Energy Environ. Sci. 11 (2018) 566–571.
[16] T. Wu, G. Chen, J. Han, R. Sun, B. Zhao, G. Zhong, Y. Yamauchi, B. Guan, Construction of three-dimensional dendritic hierarchically porous metal-organic framework nanoarchitectures via noncentrosymmetric pore-induced anisotropic assembly, J. Am. Chem. Soc. 145 (2023) 16498–16507.
[17] T.J. Bandosz, A. Policicchio, M. Florent, P.S. Poon, J. Matos, TiO_2/S-Doped carbons hybrids: analysis of their interfacial and surface features, Molecules 24 (19) (2019) 3585.
[18] C.O. Ania, P.A. Armstrong, T.J. Bandosz, F. Beguin, A.P. Carvalho, A. Celzard, E. Frackowiak, M.A. Gilarranz, K. László, J. Matos, M.F.R. Pereira, Engaging nanoporous carbons in "beyond adsorption" applications: characterization, challenges and performance, Carbon 164 (2020) 69–84.
[19] B. Yang, X. Li, Q. Zhang, X. Yang, J. Wan, G. Liao, J. Zhao, R. Wang, J. Liu, R. D. Rodriguez, X. Jia, Ultrathin porous carbon nitride nanosheets with well-tuned band structures via carbon vacancies and oxygen doping for significantly boosting H_2 production, Appl. Catal. B Environ. 314 (2022) 121521.
[20] Q. You, C. Zhang, M. Cao, B. Wang, J. Huang, Y. Wang, S. Deng, G. Yu, Defects controlling, elements doping, and crystallinity improving triple-strategy modified carbon nitride for efficient photocatalytic diclofenac degradation and H_2O_2 production, Appl. Catal. B Environ. 321 (2023) 121941.
[21] P. Xia, M. Antonietti, B. Zhu, T. Heil, J. Yu, S. Cao, Designing defective crystalline carbon nitride to enable selective CO_2 photoreduction in the gas phase, Adv. Funct. Mater. 29 (2019) 1900093.
[22] Q. Liang, Z. Li, Z.-H. Huang, F. Kang, Q.-H. Yang, Holey graphitic carbon nitride nanosheets with carbon vacancies for highly improved photocatalytic hydrogen production, Adv. Funct. Mater. 25 (2015) 6885–6892.
[23] S. An, G. Zhang, K. Li, Z. Huang, X. Wang, Y. Guo, J. Hou, C. Song, X. Guo, Self-supporting 3D carbon nitride with tunable n → π* electronic transition for enhanced solar hydrogen production, Adv. Mater. 33 (2021) 2104361.
[24] L. Lin, H. Ou, Y. Zhang, X. Wang, Tri-s-triazine-Based crystalline graphitic carbon nitrides for highly efficient hydrogen evolution photocatalysis, ACS Catal. 6 (6) (2016) 3921–3931.
[25] B. Zhai, H. Li, G. Gao, Y. Wang, P. Niu, S. Wang, L. Li, A crystalline carbon nitride based near-infrared active photocatalyst, Adv. Funct. Mater. 32 (2022) 2207375.
[26] Q. Guo, Y. Wu, L. Xia, X.-F. Yu, K. Zhang, Y. Du, L. Zhang, H. Tang, J. Cheng, J. Shang, Y. Peng, Z. Li, X. Man, X. Yang, Stitching electron localized heptazine units with "carbon patches" to regulate exciton dissociation behavior of carbon nitride for photocatalytic elimination of petroleum hydrocarbons, Chem. Eng. J. 452 (2023) 139092.
[27] Z. Wang, G. Ding, J. Zhang, X. Lv, P. Wang, L. Shuai, C. Li, Y. Ni, G. Liao, Critical role of hydrogen bonding between microcrystalline cellulose and g-C_3N_4 enables highly efficient photocatalysis, Chem. Commun. 60 (2) (2024) 204–207.
[28] G. Zhang, Y. Xu, C. He, P. Zhang, H. Mi, Oxygen-doped crystalline carbon nitride with greatly extended visible-light-responsive range for photocatalytic H_2 generation, Appl. Catal. B Environ. 283 (2021) 119636.
[29] Z. Mo, X. Zhu, Z. Jiang, Y. Song, D. Liu, H. Li, X. Yang, Y. She, Y. Lei, S. Yuan, H. Li, L. Song, Q. Yan, H. Xu, Porous nitrogen-rich g-C_3N_4 nanotubes for efficient photocatalytic CO_2 reduction, Appl. Catal. B Environ. 256 (2019) 117854.
[30] C. Liang, H.-Y. Niu, H. Guo, C.-G. Niu, D.-W. Huang, Y.-Y. Yan, H.-Y. Liu, B.-B. Shao, H.-P. Feng, Insight into photocatalytic nitrogen fixation on graphitic carbon nitride: defect-dopant strategy of nitrogen defect and boron dopant, Chem. Eng. J. 396 (2020) 125395.
[31] Y. Deng, L. Li, H. Zeng, R. Tang, Z. Zhou, Y. Sun, C. Feng, D. Gong, J. Wang, Y. Huang, Unveiling the origin of high-efficiency charge transport effect of C_3N_5/C_3N_4 homojunction for activating peroxymonosulfate to degrade atrazine under visible light, Chem. Eng. J. 457 (2023) 141261.
[32] B. Yang, J. Han, Q. Zhang, G.F. Liao, W.J. Cheng, G.X. Ge, J.C. Liu, X.D. Yang, R. J. Wang, X. Jia, Carbon defective g-C_3N_4 thin-wall tubes for drastic improvement of photocatalytic H_2 production, Carbon 202 (2023) 348–357.
[33] J. Matos, M. Hofman, R. Pietrzak, Synergy effect in the photocatalytic degradation of methylene blue on a suspended mixture of TiO_2 and N-containing carbons, Carbon 54 (2013) 460–471.
[34] P. Zhang, Y. Tong, Y. Liu, J.J.M. Vequizo, H. Sun, C. Yang, A. Yamakata, F. Fan, W. Lin, X. Wang, W. Choi, Heteroatom dopants promote two-electron O_2 reduction for photocatalytic production of H_2O_2 on polymeric carbon nitride, Angew. Chem. Int. Ed. 59 (2020) 16209–16217.
[35] J. Zhilin, C. Rongsheng, Y. Wanneng, L. Ping, D. Chung-Li, H. Yu-Cheng, S. Xilin, S. B. Denys, L. Yiming, Z. Yukun, Y. Dongjiang, Confined Fe single atomic sites on (100) plane of anatase TiO_2 nanofibers boost white LED driven Fenton-like norfloxacin degradation, J. Clean. Prod. 382 (2022) 135161.
[36] Z. Ji, R. Cai, W. Ye, P. Lu, C.-L. Dong, Y.-C. Huang, X. She, D.S. Butenko, Y. Liu, Y. Zhu, D. Yang, Confined Fe single atomic sites on (100) plane of anatase TiO_2 nanofibers boost white LED driven Fenton-like norfloxacin degradation, J. Clean. Prod. 382 (2023) 135161.
[37] Q. Zhang, G. Liao, B. Yang, Y. Zhang, G. Ge, A. Lipovka, J. Liu, R.D. Rodriguez, X. Yang, X. Jia, Structural reorganization of ultrathin g-C_3N_4 nanosheets for significantly boosting wide-spectrum-driven CO_2 photoreduction, Appl. Surf. Sci. 638 (2023) 157989.
[38] L. Chen, Y. Wang, S. Cheng, X. Zhao, J. Zhang, Z. Ao, C. Zhao, B. Li, S. Wang, S. Wang, H. Sun, Nitrogen defects/boron dopants engineered tubular carbon nitride for efficient tetracycline hydrochloride photodegradation and hydrogen evolution, Appl. Catal. B Environ. 303 (2022) 120932.
[39] X. Yuan, S. Qu, X. Huang, X. Xue, C. Yuan, S. Wang, L. Wei, P. Cai, Design of core-shelled g-C_3N_4@ZIF-8 photocatalyst with enhanced tetracycline adsorption for boosting photocatalytic degradation, Chem. Eng. J. 416 (2021) 129148.
[40] Z. Lu, C. Li, J. Han, L. Wang, S. Wang, L. Ni, Y. Wang, Construction OD/2D heterojunction by highly dispersed Ni_2P QDs loaded on the ultrathin g-C_3N_4 surface towards superhigh photocatalytic and photoelectric performance, Appl. Catal. B Environ. 237 (2018) 919–926.
[41] W. Li, Z. Wei, Y. Sheng, J. Xu, Y. Ren, J. Jing, J. Yang, J. Li, Y. Zhu, Dual cocatalysts synergistically promote perylene diimide polymer charge transfer for enhanced photocatalytic water oxidation, ACS Energy Lett. 8 (6) (2023) 2652–2660.
[42] Y. Zhu, A. Sikandaier, Y. Zhang, X. Wang, B. Du, J. Xue, Y. Sun, P. Lu, D. Yang, FeOx@FeP heterostructure: surface phosphorization toward efficient photocatalytic Fenton-like norfloxacin removal, Environ. Funct. Mater. 1 (2022) 230–238.
[43] G. Liao, C. Li, S.-Y. Liu, B. Fang, H. Yang, Emerging frontiers of Z-scheme photocatalytic systems, Trends Chem. 4 (2) (2022) 111–127.
[44] T.J. Bandosz, J. Matos, M. Seredych, M.S.Z. Islam, R. Alfano, Photoactivity of S-doped nanoporous activated carbons: a new perspective for harvesting solar energy on carbon-based semiconductors, Appl. Catal., A 445–446 (2012) 159–165.
[45] S. Zhang, S. Song, P. Gu, R. Ma, D. Wei, G. Zhao, T. Wen, R. Jehan, B. Hu, X. Wang, Visible-light-driven activation of persulfate over cyano and hydroxyl group co-modified mesoporous g-C3N4 for boosting bisphenol A degradation, J. Mater. Chem. A 7 (10) (2019) 5552–5560.
[46] G. Liao, C. Li, X. Li, B. Fang, Emerging polymeric carbon nitride Z-scheme systems for photocatalysis, Cell Rep. Phys. Sci. 2 (3) (2021) 100355.
[47] G. Liao, Y. He, H. Wang, B. Fang, N. Tsubaki, C. Li, Carbon neutrality enabled by structure-tailored zeolite-based nanomaterials, Device 1 (5) (2023) 100173.
[48] J. Tian, X. Cao, T. Sun, J. Fan, H. Miao, Z. Chen, D. Li, E. Liu, Y. Zhu, S-scheme $Co_3(PO_4)_2$/Twinned-$Cd_{0.5}Zn_{0.5S}$ homo-heterojunction for enhanced photocatalytic H_2 evolution, Chem. Eng. J. 471 (2023) 144587.
[49] T. Sun, J. Wang, X. Chi, Y. Lin, Z. Chen, X. Ling, C. Qiu, Y. Xu, L. Song, W. Chen, C. Su, Engineering the electronic structure of MoS_2 nanorods by N and Mn dopants for ultra-efficient hydrogen production, ACS Catal. 8 (8) (2018) 7585–7592.
[50] G. Liao, Y. Gong, L. Zhang, H. Gao, G.-J. Yang, B. Fang, Semiconductor polymeric graphitic carbon nitride photocatalysts: the "holy grail" for the photocatalytic hydrogen evolution reaction under visible light, Energy Environ. Sci. 12 (7) (2019) 2080–2147.
[51] X. Wang, Y. Han, W. Li, J. Li, S. Ren, M. Wang, G. Han, J. Yu, Y. Zhang, H. Zhao, Doped carbon dots enable highly efficient multiple-color room temperature phosphorescence, Adv. Opt. Mater. 2301962.
[52] Y. Zhu, Y. Zhuang, L. Wang, H. Tang, X. Meng, X. She, Constructing 0D/1D Ag_3PO_4/TiO_2 S-scheme heterojunction for efficient photodegradation and oxygen evolution, Chin, J. Catal. 43 (10) (2022) 2558–2568.
[53] X. Xiao, Y. Gao, L. Zhang, J. Zhang, Q. Zhang, Q. Li, H. Bao, J. Zhou, S. Miao, N. Chen, J. Wang, B. Jiang, C. Tian, H. Fu, A promoted charge separation/transfer system from Cu single atoms and C_3N_4 layers for efficient photocatalysis, Adv. Mater. 32 (2020) 2003082.
[54] B. Yang, J.J. Zhao, W.D. Yang, X.Y. Sun, R.J. Wang, X. Jia, A step-by-step synergistic stripping approach toward ultra-thin porous g-C_3N_4 nanosheets with

high conduction band position for photocatalystic CO_2 reduction, J. Colloid Interface Sci. 589 (2021) 179–186.
[55] Z. Yukun, L. Chunxiao, Y. Zhuocheng, R. Jun, Y. Xianfeng, D. Chung-Li, L. Hongwei, C. Rongsheng, H. Yu-Cheng, T. Wolfgang, S. Shaohua, Y. Dongjiang, A [001]-Oriented hittorf's phosphorus nanorods/polymeric carbon nitride heterostructure for boosting wide-spectrum-responsive photocatalytic hydrogen evolution from pure water, Angew. Chem. Int. Ed. 59 (2019) 868–873.
[56] Y. Zhu, C. Lv, Z. Yin, J. Ren, X. Yang, C.-L. Dong, H. Liu, R. Cai, Y.-C. Huang, W. Theis, S. Shen, D. Yang, 001 -oriented hittorf's phosphorus nanorods/polymeric carbon nitride heterostructure for boosting wide-spectrum-responsive photocatalytic hydrogen evolution from pure water, Angew. Chem. Int. Ed. 59 (2) (2020) 868–873.
[57] C. Fu, M. Zhao, X. Chen, G. Sun, C. Wang, Q. Song, Unraveling the dual defect effects in C_3N_5 for piezo-photocatalytic degradation and H_2O_2 generation, Appl. Catal. B Environ. 332 (2023) 122752.
[58] M. Cui, K. Cui, X. Liu, X. Chen, Z. Guo, Y. Chen, C.-x. Li, Insights into the photocatalytic peroxymonosulfate activation over defective boron-doped carbon nitride for efficient pollutants degradation, J. Hazard Mater. 418 (2021) 126338.
[59] E. Hu, Q. Chen, Q. Gao, X. Fan, X. Luo, Y. Wei, G. Wu, H. Deng, S. Xu, P. Wang, L. Liu, R. He, X. Chen, W. Zhu, Y. Zhu, Cyano-functionalized graphitic carbon nitride with adsorption and photoreduction isosite achieving efficient uranium extraction from seawater, Adv. Funct. Mater. 2312215.
[60] L. Yan, W. Xiao, Y. Wanneng, S.B. Denys, L. Ping, C. Qian, C. Rongsheng, S. Jin, Z. Yukun, Y. Dongjiang, FeOx nanoclusters decorated TiO_2 for boosting white LED driven photocatalytic Fenton-like norfloxacin degradation, Sep. Purif. Technol. 303 (2022) 122194.
[61] L.F. Velasco, R.J. Carmona, J. Matos, C.O. Ania, Performance of activated carbons in consecutive phenol photooxidation cycles, Carbon 73 (2014) 206–215.
[62] Z. Wang, E. Almatrafi, H. Wang, H. Qin, W. Wang, L. Du, S. Chen, G. Zeng, P. Xu, Cobalt single atoms anchored on oxygen-doped tubular carbon nitride for efficient peroxymonosulfate activation: simultaneous coordination structure and morphology modulation, Angew. Chem. Int. Ed. 61 (2022) e202202338.
[63] Y. Meng, Z. Li, J. Tan, J. Li, J. Wu, T. Zhang, X. Wang, Oxygen-doped porous graphitic carbon nitride in photocatalytic peroxymonosulfate activation for enhanced carbamazepine removal: performance, influence factors and mechanisms, Chem. Eng. J. 429 (2022) 130860.
[64] T.J. Bandosz, A. Policicchio, M. Florent, W. Li, P.S. Poon, J. Matos, Solar light-driven photocatalytic degradation of phenol on S-doped nanoporous carbons: the role of functional groups in governing activity and selectivity, Carbon 156 (2020) 10–23.
[65] H. Wang, C. Cao, D. Li, Y. Ge, R. Chen, R. Song, W. Gao, X. Wang, X. Deng, H. Zhang, B. Ye, Z. Li, C. Li, Achieving high selectivity in photocatalytic oxidation of toluene on amorphous BiOCl nanosheets coupled with TiO_2, J. Am. Chem. Soc. 145 (2023) 16852–16861.
[66] C. Li, H. Lu, G. Ding, Q. Li, G. Liao, Recent advances on g-C_3N_4 based Z-scheme photocatalysts for organic pollutant removal, Catal. Sci. Technol. 13 (2023) 2877–2898.
[67] J. Matos, J. Arcibar-Orozco, P.S. Poon, G. Pecchi, J.R. Rangel-Mendez, Influence of phosphorous upon the formation of DMPO-OH and POBN-$O_2^{\bullet-}$ spin-trapping adducts in carbon-supported P-promoted Fe-based photocatalysts, J. Photochem. Photobiol., A 391 (2020) 112362.
[68] Z. Weng, Y. Lin, B. Han, X. Zhang, Q. Guo, Y. Luo, X. Ou, Y. Zhou, J. Jiang, Donor-acceptor engineered g-C_3N_4 enabling peroxymonosulfate photocatalytic conversion to $^1O_2$ with nearly 100% selectivity, J. Hazard Mater. 448 (2023) 130869.
[69] J. Huang, D. Li, R. Li, Q. Zhang, T. Chen, H. Liu, Y. Liu, W. Lv, G. Liu, An efficient metal-free phosphorus and oxygen co-doped g-C_3N_4 photocatalyst with enhanced visible light photocatalytic activity for the degradation of fluoroquinolone antibiotics, Chem. Eng. J. 374 (2019) 242–253.
[70] H. Chi, J. Wan, Y. Ma, Y. Wang, M. Huang, X. Li, M. Pu, ZSM-5-(C@Fe) activated peroxymonosulfate for effectively degrading ciprofloxacin: in-depth analysis of degradation mode and degradation path, J. Hazard Mater. 398 (2020) 123024.
[71] Q. Ji, X. Cheng, Y. Wu, W. Xiang, H. He, Z. Xu, C. Xu, C. Qi, S. Li, L. Zhang, S. Yang, Visible light absorption by perylene diimide for synergistic persulfate activation towards efficient photodegradation of bisphenol A, Appl. Catal. B Environ. 282 (2021) 119579.
[72] W. Li, Y. Zhang, X. Cheng, J. Wang, B. Yang, H. Guo, Amino-modified metal-organic frameworks as peroxymonosulfate catalyst for bisphenol AF decontamination: ROS generation, degradation pathways, and toxicity evaluation, Sep. Purif. Technol. 282 (2022) 119967.
[73] B. Yang, J. Zheng, W. Li, R. Wang, D. Li, X. Guo, R.D. Rodriguez, X. Jia, Engineering Z-scheme TiO_2-OV-BiOCl via oxygen vacancy for enhanced photocatalytic degradation of imidacloprid, Dalton Trans. 49 (2020) 11010–11018.
[74] M. Bourgin, F. Violleau, L. Debrauwer, J. Albet, Ozonation of imidacloprid in aqueous solutions: reaction monitoring and identification of degradation products, J. Hazard Mater. 190 (2011) 60–68.
[75] X. Wang, Z. Chen, Y. He, X. Yi, C. Zhang, Q. Zhou, X. Xiang, Y. Gao, M. Huang, Activation of persulfate-based advanced oxidation processes by 1T-MoS_2 for the degradation of imidacloprid: performance and mechanism, Chem. Eng. J. 451 (2023) 138575.
[76] R. Tang, H. Zeng, Y. Deng, S. Xiong, L. Li, Z. Zhou, J. Wang, L. Tang, Dual modulation on peroxymonosulfate activation site and photocarrier separation in carbon nitride for efficient photocatalytic organics degradation: efficacy and mechanism evaluation, Appl. Catal. B Environ. 336 (2023) 122918.
[77] A. Yaghoot-Nezhad, S. Waclawek, S. Madihi-Bidgoli, A. Hassani, K.-Y.A. Lin, F. Ghanbari, Heterogeneous photocatalytic activation of electrogenerated chlorine for the production of reactive oxygen and chlorine species: a new approach for Bisphenol A degradation in saline wastewater, J. Hazard Mater. 445 (2023) 130626.